ARMA 19-1617

Effects of spatial variation of cluster entry friction on hydraulic fracture propagation in multistage fracturing

Nikolskiy, D.
EPFL, Lausanne, Switzerland
Lecampion, B.
EPFL, Lausanne, Switzerland
Pourpak, H.
Total E&P, Pau, France
Onaisi, A.
Total E&P, Pau, France

ABSTRACT: In this contribution, we explore different aspects of the multi-stage fracturing process such as stress interaction between growing hydraulic fractures, perforation and near-wellbore tortuosity effects as well as the wellbore flow dynamics using a fit-for-purpose numerical model, which accounts for the full fluid-solid coupling nature of hydraulic fracture propagation, stress interactions between multiple growing fractures, and the coupling with the wellbore flow via entry friction. We restrict the hydraulic fractures to be fully contained in the reservoir. After presenting several verifications of this model, we investigate the effect of spatial variation of the entry friction associated with the near-wellbore fracture tortuosity. We show that, although large perforation friction helps to equalize the fluid partitioning between fractures, the pressure drop along the length of the stage and, more importantly, spatial variations of the entry friction due to near-wellbore fracture tortuosity have a more pronounced adverse effect on the fluid partitioning.

1. INTRODUCTION

In multi-stage fracturing where the aim is to propagate simultaneously several hydraulic fractures from different perforation clusters along the well (between two to six or more), the actual flow rate entering each fracture at any given time during the stimulation is actually unknown. The goal is - of course - to achieve an even splitting of the surface pump rate between all propagating fractures. However, this is difficult to achieve in practice (Bunger and Lecampion, 2017; Lecampion *et al.*, 2015). The success of the operation depends on both the stress interaction between growing hydraulic fractures, the perforation / near-wellbore tortuosity effects, the possible stress and material heterogeneities encountered along the length of the stage as well as the wellbore flow dynamics.

In this contribution, we explore these different aspects of the multi-stage fracturing process using a fit-for-purpose numerical model following previous contributions (Olson and Taleghani (2009); Bunger and Peirce (2014); Lecampion and Desroches (2015b); Kresse and Weng (2018); Kumar and Ghassemi (2016) to cite only a few). In particular, the model accounts for the full fluid-solid coupling nature of hydraulic fracture propagation, stress interactions between multiple growing fractures, and the coupling with the wellbore flow via entry friction. We restrict the hydraulic fractures to be fully contained in the reservoir (e.g. of constant height) - a limiting case corresponding to a large in-situ stress (or / and material properties) contrast between the reservoir and its bounding layers. However, the fractures can curve in the horizontal plane due to stress interactions and in-situ stress heterogeneities (see Fig. 1). We pay particular attention to the coupling between wellbore flow and the simultaneous propagation of hydraulic fractures - additional non-linearities that must be properly solved as they directly control fluid partitioning. We restrict our discussion here to the zero leak-off case for clarity.

After presenting several verifications of this numerical model, we move to define and study numerically the parameters controlling the growth of multiple hydraulic fractures during a pumping stage. We perform a series of numerical simulations on 3 and 4 clusters. Our results confirm that in

any case large entry friction allows to balance more evenly the fluid partitioning between the different fractures. More importantly, our results indicate that the pressure drop along the length of the stage has a more detrimental effect than the stress interactions between the growing fractures. Then we investigate the effect of spatial variation of the entry friction term (pressure drop vs. entry rate) associated with the near-wellbore fracture tortuosity (thus indirectly accounting for near-wellbore stress heterogeneity) using well established relations between the entering rate and the entry pressure drop (Lagrone and Rasmussen, 1963; Economides and Nolte, 2000) . We perform simulations for several realizations for a specific type of heterogeneity statistics. For each realization, we study the effects of perforation friction, stress interactions, and stage length, and then discuss averaged results over each set of realizations. Our results indicate that even for low variation of near-wellbore fracture tortuosity between clusters, standard deviation of the flow rate entering different fractures incrases significantly compared to the spatially homogeneous case.

2. MODEL DESCRIPTION

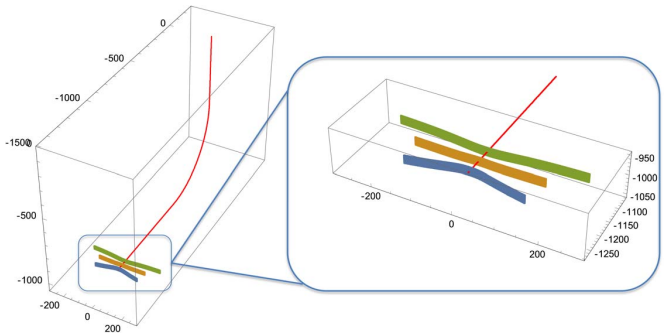

Fig. 1: A schematic view of multiple height contained (blade-like) hydraulic fractures growing simultaneously from a horizontal well. Scales in meters.

2.1. Solid deformation

In the case of an uniform isotropic elastic medium, the governing equations of elasticity allow for an integral representation. Superposing the interaction stress (normal and shear tractions induced by displacement discontinuities (DD) distributed over the fracture surface) with the in-situ stress field $\sigma^o(\mathbf{x})$, $\tau^o(\mathbf{x})$ and taking into account the balance of normal traction with the net fluid pressure $p(\mathbf{x})-\sigma^o(\mathbf{x})$, we obtain the following set of boundary integral equations on all fracture surface S (see e.g. Mogilevskaya (2014)):

$$\begin{aligned} p(\mathbf{x})-\sigma^o(\mathbf{x}) &= \int_S \big(K^{nn}(\mathbf{x}-\mathbf{x}',H)\delta^n(\mathbf{x}') \\ &\quad +K^{ns}(\mathbf{x}-\mathbf{x}',H)\delta^s(\mathbf{x}')\big)\,d\mathbf{x}' \\ -\tau^o(\mathbf{x}) &= \int_S \big(K^{sn}(\mathbf{x}-\mathbf{x}',H)\delta^n(\mathbf{x}') \\ &\quad +K^{ss}(\mathbf{x}-\mathbf{x}',H)\delta^s(\mathbf{x}')\big)\,d\mathbf{x}' \end{aligned} \tag{1}$$

where δ^n is normal DD (fracture opening), δ^s is the shear DD (shear slip). The right-hand side of eq.1 represents the interaction stress.

The elastic kernel $K^{kl}(\mathbf{x}-\mathbf{x}',H)$, $k,l=n,s$ used here corresponds to a simplified approximation obtained from the full 3 dimensional kernel for a rectangular DD with appropriate corrections factors to account for a given fracture height as suggested by Wu and Olson - see Wu and Olson (2015). It is chosen here as a computational cheap alternative to the direct integration of the full 3D kernel (the fundamental solution corresponding to the so-called double layer potential) over the height of the fracture(s). Normal and shear isplacements (δ^n, δ^s) and the corresponding stresses are taken in the horizontal mid-plane. It is however important to keep in mind that such an approximate kernel leads to erroneous stress predictions (about 10-15% difference compared to a full 3D scheme) when the spacing between hydraulic fractures are lower than 0.25 the fracture height according to Wu and Olson (2015). We note that an interesting alternative to the simplified 3D kernel used here is to enforce the hypothesis of an elliptical cross section of the fractures as presented in Protasov *et al.* (2018). The latter approach will likely lead to better approximation for lower spacing to height ratios.

2.2. Fluid flow in fracture

The mass conservation averaged over the width of the I-th fracture in the absence of leak-off reduces to

$$\frac{\partial w}{\partial t}+c_f w\frac{\partial p}{\partial t}+\frac{\partial q}{\partial s}+v_{leak-off}=\widetilde{Q}_I(t)\delta(s-s_{well}) \tag{2}$$

where s is the curvilinear coordinate along the fracture footprint (in horizontal direction), c_f is the fluid compressibility, p is the fluid pressure, $w=w_o+\delta^n$ is the total hydraulic width of the fracture where w_o is a small initial aperture only active in the initial flaw, $\widetilde{Q}_I=\frac{Q_I}{H}$ is the entry volume rate per unit fracture height, s_{well} denotes the well location on the fracture, and $\delta(s-s_{well})$ is the Kronecker symbol. We note that the effect of fluid compressibility is negligible during propagation. We include it here to properly account for the initial pressurization of fracture at the beginning of the stimulation. Assuming laminar flow inside the fracture, the width-averaged fluid momentum balance reduces

to Poiseuille's law. Then the local fluid flux $q(s)$ is given as

$$q(s) = -\frac{w^3}{12\mu}\frac{\partial p}{\partial s} \tag{3}$$

where μ is the dynamic viscosity of the fracturing fluid.

2.3. Fluid flow in the wellbore

In the simultaneous hydraulic fracture propagation problem, a key part is to properly account for fluid partitioning between the different fractures therefore one needs to model fluid flow inside the wellbore. Neglecting inertial effects that may be associated with short transient pressure changes (water hammer etc.), the mass and momentum balance in the wellbore after integration over the wellbore cross-section are simplified in terms of the curvilinear coordinate s along the well trajectory as:

$$Ac_f\frac{\partial p}{\partial t} + \frac{\partial AV}{\partial s} + AVc_f\frac{\partial p}{\partial s} = Q_{pump}(t)\delta(s) - \sum_{I=1}^{N} Q_I(t)\delta(s-s_I) \tag{4}$$

and

$$\frac{\partial p}{\partial s} = -\frac{2\pi a}{A}\frac{f(Re,\varepsilon)}{4}\frac{\rho V|V|}{2} + \rho g\sin\theta(s) \tag{5}$$

where a is the wellbore radius, A is the cross-section area ($A=\pi a^2$), ρ the fracturing fluid density, c_f is the fluid compressibility, V is the average fluid velocity, $Q_{pump}(t)$ is the volumetric pump rate at the well head (i.e. at $s=0$), $Q_I(t)$ is the flow rate entering the I-th fracture, $f(Re,\varepsilon)$ is the Darcy friction factor depending on the Reynolds number $Re=\frac{2\rho a|V|}{\mu}$ and surface roughness ε.

2.4. Coupling between wellbore and fracture flow

We account for a local pressure drop due to entry friction between the wellbore and the fracture. Following accepted relation for such entry friction (Lagrone and Rasmussen, 1963; Economides and Nolte, 2000), we relate the pressure drop between the wellbore and the fracture I and the fluid flux entering the fracture I as follow:

$$p_{w,I} - p_{in,I} = f_p\,Q_I^2 + f_t\,Q_I^\beta \tag{6}$$

where $p_{w,I}=p(s_I)$ is the fluid pressure inside the wellbore at the location of the perforations of fracture I and $p_{in,I}$ is the fluid pressure at the inlet of the fracture I. Q_I is the total fluid flux entering the fracture I which is an unknown function of time resulting from the fluid partitioning between the different fractures. The first quadratic term in eq.(6) corresponds to classic turbulent pressure drop associated with the perforations connecting the fracture to the well. The coefficient f_p for n_p perforations per well circumference of diameter D_p can be estimated using an empirical formula $f_p = 0.807249\,\frac{\rho}{n_p^2 D_p^2 C^2}$ (see e.g. Crump and Conway (1988)) where the dimensionless discharge coefficient C is typically between 0.5 and 0.9. The second term in eq.(6) is added to account for additional pressure drop associated with near-wellbore fracture tortuosity; $f_{t,i}$ and β_i can be estimated from step-down tests - see Economides and Nolte (2000); Lecampion and Desroches (2015b); Bunger and Lecampion (2017) for more details.

2.5. Fracture propagation criteria / tip asymptotic

Under the hypothesis of linear elastic fracture mechanics (LEFM), the quasi-static fracture propagation condition reduces to $K_I = K_{Ic}$ where K_{Ic} is the rock fracture toughness (yet, K_I can be less than K_{Ic} for an arrested fracture). Locally at the fracture tip, we thus assume condition of pure mode I, such that the fracture width of a propagating fracture result in the well-known linear elastic fracture asymptote:

$$w = \sqrt{32/\pi}\,\frac{K_{Ic}}{E'}\sqrt{\ell - s}; \qquad \ell - s \ll \ell \tag{7}$$

In fact, this near-tip behavior may be visible only over a very small characteristic length for a propagating hydraulic fracture where a outer viscous asymptotes may dominate ($l_{mk}=\frac{K'^6}{E'^4\mu'^2V_{tip}^2}$) Garagash *et al.* (2011). This renders the use of a sole linear elastic fracture mechanics criteria extremely demanding computationally as the mesh size must then resolve the small lengthscale where the LEFM asymptote is valid (see Lecampion *et al.* (2013, 2018) for discussion). For this reason, we use a so-called "universal" tip asymptote covering toughness-, viscosity-, and leakoff-dominated regimes near the fracture tip - see Garagash *et al.* (2011); Dontsov and Peirce (2015, 2017).

We account for fracture curving (mixed mode) using a maximum tensile stress direction criteria - which give similar predictions that the principle of local symmetry (minimum K_{II}) (Pham *et al.*, 2017).

2.6. Initial / boundary conditions

Initially, prior to the start of the injection, at time $t=0$, the well is under hydrostatic pressure: $p(s,t=0)=\rho\,g\,z(s)$ and $V(s,t=0)=0$. At the scale of this model which assumes a constant fracture height, the details of fracture initiation from the perforations can not be properly captured. We simply assume the existence of a small pre-existing flaw transverse to the well axis at the location of each perforation clusters. In other words, each fractures are pre-initiated with a initial length ($\ell_I(t=0)=L_o$) and assumed initially closed prior to the start of injection at $t=0$. The fluid flux at the end of stage (at the location of the bridge plug) is assumed

to be zero at all times $V(s = S_{plug}, t) = 0$, while we assume that the surface pump rate is prescribed $Q(s = 0, t)$. We will notably restrict our discussion to the case of a constant pump rate.

2.7. Notes on numerical scheme (discrete equations)

For each time step, the elasto-hydrodynamics equations are solved iteratively assuming the fracture tips locations (these are iterated for in external loop). So, while iterating for $\delta^n(x)$, $\delta^s(x)$ and $p(x)$ within a time step, the fracture length is fixed. Yet, the opening δ^n in the tip region is imposed to enforce mass conservation using the universal HF tip asymptote.

The elasticity equations are discretized using piece-wise constant (P0) displacement discontinuity elements - see Crouch and Starfield (1983); Wu and Olson (2015). The fracture opening and shear as well as the tractions (fluid pressure and in-situ stress) are given in the middle of each element. The lubrication equation (2) is integrated over an element thus resulting in a Finite Volume discretization. For a given locations of fracture tips (thus, fracture footprint fixed), the mixed elasto-hydrodynamics system is solved via fixed-point iterations.

To find the location of each fracture tip we use a 1D implicit level set approach (see e.g. Peirce (2016); Dontsov and Peirce (2017) for details) - inversion of the asymptote for opening known at a given cell, the so-called "ribbon" cell, which we set behind to the one that contained the tip at the previous time step. Since the universal tip asymptote is given as an implicit function, the location of the tip is found from the opening at the corresponding "ribbon" element iteratively using Brent technique.

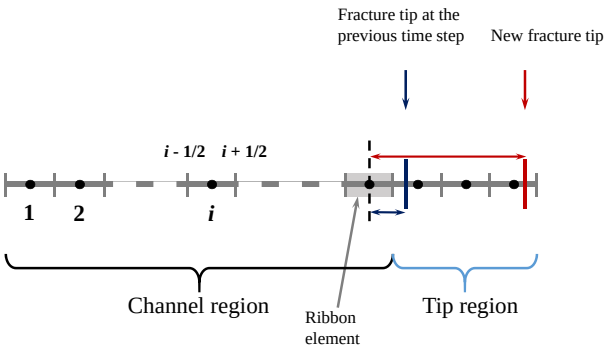

Fig. 2: Schematic of the fracture mesh to illustrate fracture propagation: tip region and ribbon element and evolution of the fracture tip position over a time step. The ribbon element allows to couple the tip region (where the solution follows the near-tip hydraulic fracture asymptotes - see Garagash *et al.* (2011)) with the rest of the fracture (e.g. channel region). The number of elements in the tip region can increase during a propagation step. Figure adapted from Lecampion and Desroches (2015b).

To determine the direction of propagation at each time step we minimize the dot product of the proposed direction and the 1st principal stress direction at finite distance from the tip node (we use 0.5 - 2.5 size of an element). This is done explicitly at the end of each time step using the same Brent method routine.

The mass balance equation in the wellbore (4) is discretized using a Finite Volume approach similar to the one described above for the lubrication in the fracture(s). One difference is that the radius and the cross-section of the well are assumed to not change due to the well pressurization thus we do not need any hydro-mechanical coupling. Another difference is the use of Darcy friction factor approach to determine the cross-sectional conductivities in laminar, turbulent, or transient flow regimes. it is a Finite Volume scheme with piecewise-constant approximation of pressure. The discretized equation is solved by fixed-point iterations while back-substituting the cross-section-average velocity (and Reynolds number) re-calculated via eq.(5) into (4). The Darcy friction factor is also updated since it depends on the Reynolds number. In the developed code, various models for friction factor in transitional and turbulent regimes are implemented, e.g. Churchill (1977), Haaland (1983), Maximum drag reduction model for slickwater injection, Yang and Dou model - an approximation of Nikuradze experimental data (see Nikuradse (1950), Yang and Dou (2010); Yang and Joseph (2009); Yang (2009)) with Reichert or Gauckler-Manning-Strickler asymptotes for large Reynolds numbers. Some models involve inversion of implicit functions of Reynolds number; this is performed using the same Brent solver routine (see above).

The equation of wellbore / fracture coupling, especially when considering near-wellbore fracture tortuosity, is highly nonlinear. Practically, we have observed (similarly than) that for this very stiff coupling in relation to fluid partitioning, fixed-point iterations do not necessarily converge. For this reason, we use a quasi-Newton scheme using a finite difference estimation of the Jacobian matrix (which we update only every 4 iterations of the quasi-Newton scheme for efficiency).

3. MODEL VERIFICATIONS

3.1. Toughness- and viscosity-dominated solutions (KGD geometry)

Two tests have been performed with two fractures of sufficiently large height (100 m) located far enough from each other (1000 m) to ensure that stress interaction between them is negligible. The flow rates entering both fractures were equal (wellbore flow was not considered).

The parameters for the toughness-dominated case were as follows: $E' = 10\,GPa$, $\mu = 0.01\,Pa.s$, $K_{Ic} = 2\,MPa.m^{1/2}$, Q_0 (per unit height) $= 0.0001\,m^2/s$ (which provide $\mathscr{M} = \frac{12\mu Q_0 E'^3}{K'^4} = 0.0072$). As can be seen on Fig. 3, the accuracy of the scheme is excellent.

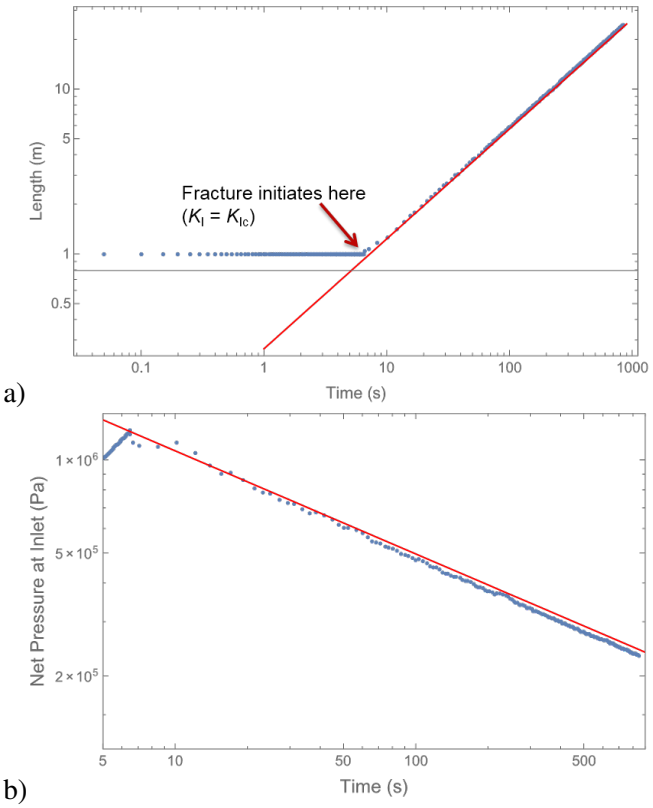

Fig. 3: Toughness-dominated fracture propagation: (a) fracture length vs. time, numerical (blue dots) vs. analytical solution (red solid line); (b) inlet pressure vs. time, numerical (blue dots) vs. analytical solution (red solid line).

For the viscosity-dominated case the parameters were as follows: $E' = 10\,GPa$, $\mu = 0.1\,Pa.s$, $K_{Ic} = 0.5\,MPa.m^{1/2}$, $Q_0 = 0.0001\,m^2/s$ ($\mathscr{M} = 18.5$). Fig. 4 display the corresponding results for fracture length and inlet net pressure evolution with time.

The results of both tests (toughness and viscosity dominated propagation) show good (within 3%) correspondence with analytical solutions.

3.2. KGD-PKN transition

This test was performed for the case a single hydraulic fracture of constant height $H = 10\,m$ and initial length $L_0 = 1\,m$ ensuring the injection time is long enough for the fracture to evolve to final length much larger than the height; the other used parameters were as follows: rock properties $E = 25\,GPa$, $\nu = 0.3$, $K_{Ic} = 1\,Mpa.m^{1/2}$, zero leak-off, confining stress $\sigma_h = 10\,MPa$, $\sigma_H = 12\,MPa$, injection fluid viscosity $\mu = 0.01\,Pa.s$, entry rate $Q = 0.05\,m3/s$ ($\sim 20\,BPM$).

As can be seen on Fig. 5, the scheme properly capture the

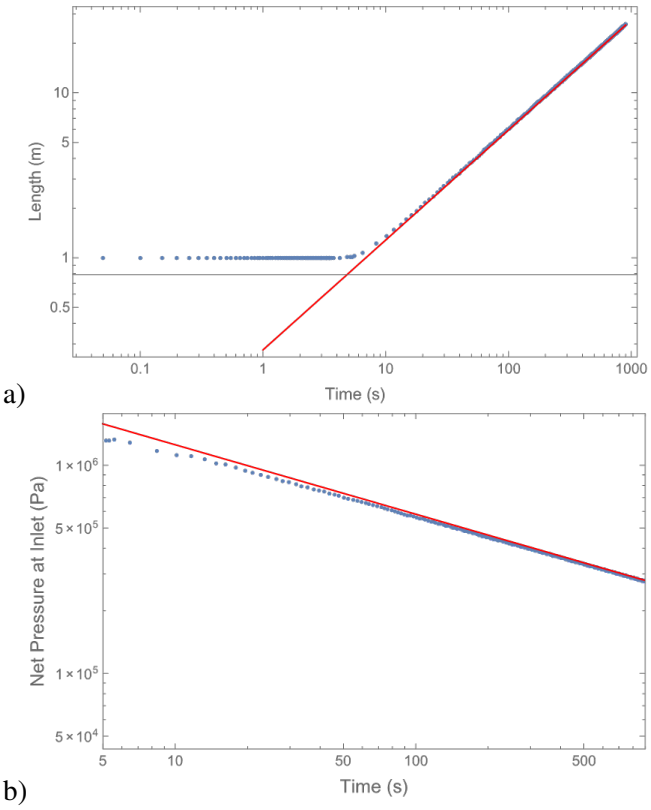

Fig. 4: Viscosity-dominated fracture propagation: (a) fracture length vs. time, numerical (blue dots) vs. analytical solution (red solid line); (b) inlet pressure vs. time, numerical (blue dots) vs. analytical solution (red solid line)

transition between the KGD geometry solution (where the height of the fracture is much larger than its length) and the PKN solution (solution for a constant height fracture very long compared to its heigth).

4. EFFECTS OF PERFORATION FRICTION ON FLUID PARTITIONING AND FRACTURE GROWTH LOCALIZATION

In this section, we report the studies of the effects of entry friction, stage length, and stress shadow on fluid partitioning and localization of fracture growth. Here we assume homogeneous perforation friction for all the clusters within the stage and neglect any wellbore tortuosity friction.

4.1. Main dimensionless parameters

We focus on the two main dimensionless parameters governing the competition between the interaction stress, the pressure gradient in the well, and the pressure drop due to the entry friction.

Following Lecampion and Desroches (2015b), the parameter Γ expresses the ratio of characteristic interaction stress σ_{int} to the pressure drop due to perforation friction at the time when the length of the fracture(s) L is of the same

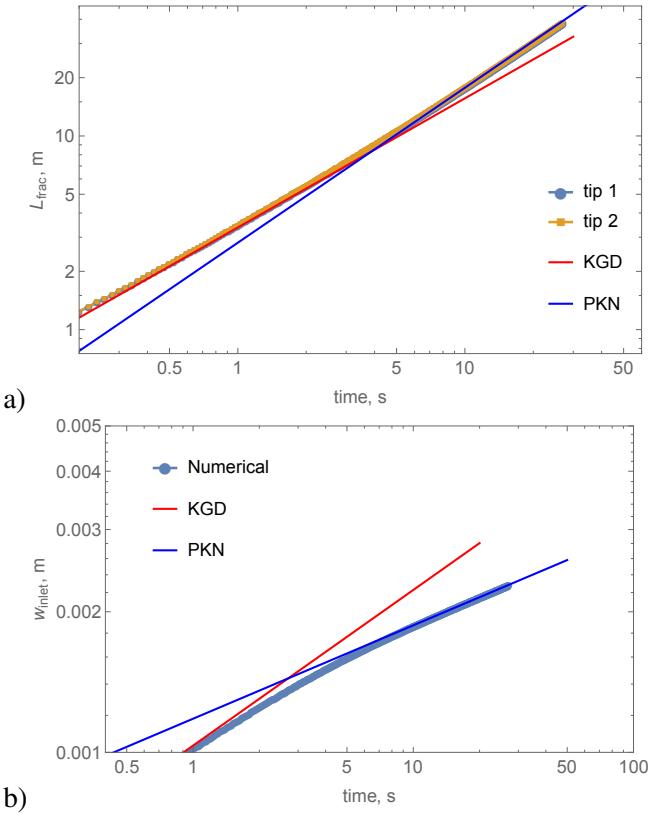

Fig. 5: KGD to PKN transition (viscosity-dominated regime), numerical vs. analytical solutions: (a) fracture length vs. time; (b) fracture inlet opening vs. time.

order as spacing S.

$$\Gamma = \frac{\sigma_{int}}{f_p Q_n^2} = \frac{E' \langle w \rangle L H}{4\pi S^3 f_p Q_n^2} = \frac{E' Q_n t}{4\pi S^3 f_p Q_n^2}$$
$$Q_n = \frac{Q_o}{N_{frac}} \tag{8}$$

The time t when the length of the fracture(s) L is of the same order as spacing S can be estimated by order of magnitude from the system parameters using the estimate of L for a specific geometry and regime of propagation. In the following, we use the estimate of L vs. t for viscosity-dominated regime in PKN geometry ($L \gg H$)

$$L \sim \left(\frac{E' Q_n^3}{4\pi^3 \mu H^4} \right)^{1/5} t^{4/5} \tag{9}$$

and the corresponding estimate of Γ (less the factor of order 1):

$$\Gamma_m = \frac{E'^{3/4} \mu^{1/4} H}{f_p{}^{7/4} n^{7/4} S^{7/4}} \tag{10}$$

The parameter Π expresses the ratio of the pressure drop between clusters in the well to the pressure drop due to perforation friction. Regarding that the pressure drop along the well is by order of magnitude $\Delta P^{(well)} \sim \rho Q_o^2 S / D^5$ and $\Delta P^{(perf)} \sim f_p (Q_o / N_{frac})^2$ we can estimate Π as

$$\Pi_\beta = \frac{\Delta P^{(well)}}{\Delta P^{(perf)}} = \frac{\rho S Q_o^2 Re^{-\beta} / D^5}{f_p (Q_o / N_{frac})^2}$$
$$= \frac{\rho S N_{frac}^2 Re^{-\beta}}{D^5 f_p}; \quad Re = \frac{\rho Q_o}{\mu D} \tag{11}$$

Here, the power exponent β is defined by the flow regime in the well and the corresponding behavior of friction factor. In the following, we consider $\beta = 1/4$ corresponding to the Blasius asymptote (see Blasius (1913)) / smooth turbulent pipe flow.

4.2. *Simultaneous fracture propagation with homogeneous perforation friction*

In these tests we considered 3 fractures initiated from the horizontal part of the well at depth of $1\,km$; the hight of the fracture was taken $H = 20\,m$; initial half-length of the fractures was $L_0 = 2.5\,m$. The following rock properties were assumed: $E = 25\,GPa$, $\nu = 0.2$, $K_{Ic} = 1\,Mpa.m^{1/2}$, zero leak-off. The other parameters are as follows: confining stress $\sigma_h = 10\,MPa$, $\sigma_H = 10.1, 12, 20\,MPa$, injection fluid viscosity $\mu = 0.01\,Pa.s$, pump rate $Q = 0.15\,m3/s$ ($0.05\,m3/s$ per fracture), entry friction f_p was the same for each cluster and took values between 10^2 and $10^9\,Pa.(s/m3)^2$. Injection time was limited to 5 minutes in all tests. To account for pressure drop between the clusters numerically, the mesh density for the well flow solver was chosen to provide 3 - 12 cells between the clusters in all considered cases of cluster spacing. The geometry of the well, location of the clusters, and a typical fracture propagation pattern can be seen in Fig. 1.

To summarize these results, let's study the effect of the most important dimensionless parameters ($\Gamma_{m'}$ and Π_β) on variation (relative standard deviation) of fractures' length and injected volumes after given time of injection.

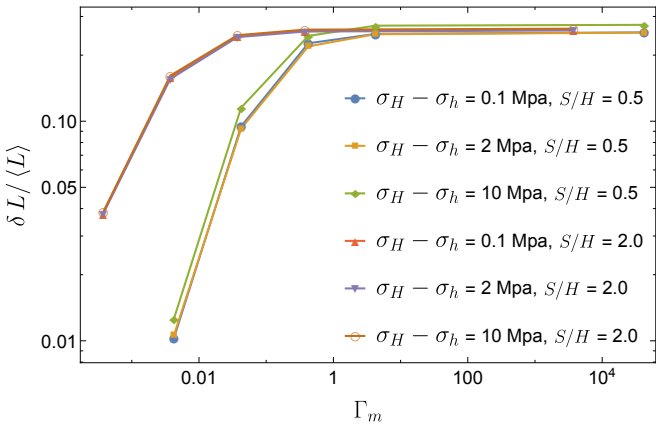

Fig. 6: Effect of parameter Γ_m on localization of fracture growth (relative standard deviation of length after 5 min. of injection).

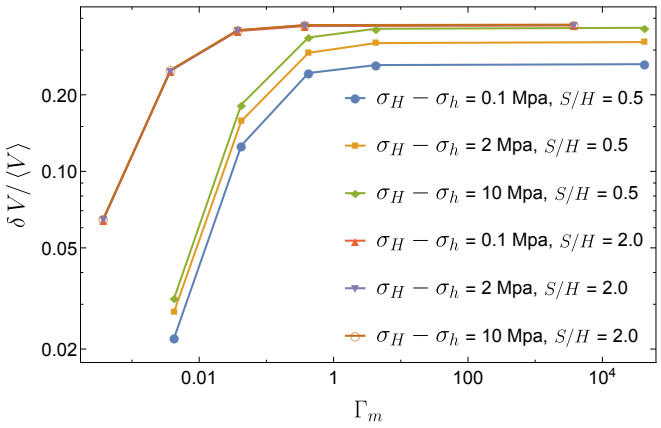

Fig. 7: Effect of parameter Γ_m on fluid partitioning (relative standard deviation of injected volume after 5 min. of injection).

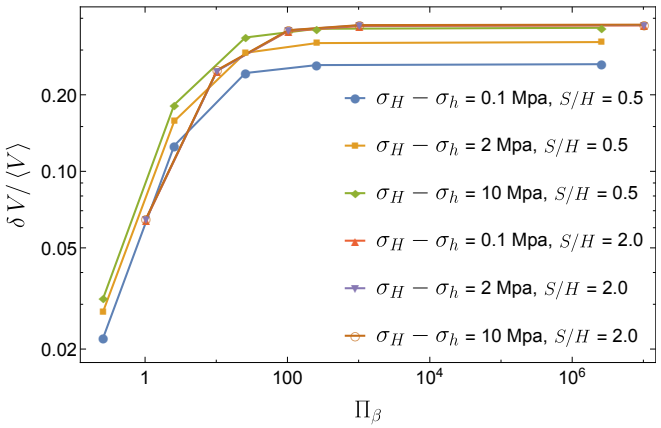

Fig. 9: Effect of parameter Π_β on fluid partitioning (relative standard deviation of injected volume after 5 min. of injection).

As one can see from Figs. 6 - 7, in general, at values of $\Gamma_m \ll 1$ fracture growth / fluid partitioning is equalized; localized growth / fluid partitioning occurs at values of $\Gamma_m > 1$; for larger Γ_m, the values of $\delta L/ < L >$ and $\delta Q/ < Q >$ stay around 25 - 30% showing some noticeable but minor effect of cluster spacing and in-situ stress contrast. Yet, the parameter Γ_m does not fully account for the effect of cluster spacing / stage length (and the corresponding pressure gradient in the well) on fracture localization. For larger spacing, localization occurs at smaller values of Γ_m.

Figs. 8 and 9 show the variation of L and Q against the parameter Π_β (scaled pressure drop between the clusters).

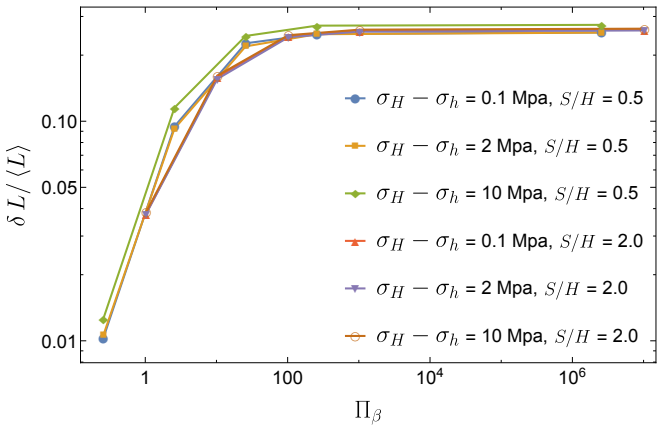

Fig. 8: Effect of parameter Π_β on localization of fracture growth (relative standard deviation of length after 5 min. of injection).

5. EFFECTS OF HETEROGENEOUS TORTUOSITY-RELATED FRICTION

In this section, we study the effect of near-wellbore stress heterogeneity (via variation of the tortuosity entry friction term f_t, see eq.(6)) on fluid partitioning and localization of fractures' propagation.

We investigated the cases of 2250 m. deep well with 3 and 4 clusters. The other parameters of the problem were as follows: Fractures' height $H = 35m$, spacing: $S = 25m$, initial length $L_o = 2.5m$ Rock properties: $E = 25GPa$, $\nu = 0.2$, $K_{Ic} = 1\,MPa\,m^{1/2}$, zero leak-off. In-situ stress: $\sigma_h = 48MPa$, $\sigma_H = 67MPa$. Injection: Slickwater (MDR friction model), fluid viscosity: $\mu = 0.05Pa\ s$, pump rate: $Q_0 = 0.19m^3/s$, duration: 10 min. Perforation friction (uniform for all clusters): $f_p = 8\cdot10^6, 8\cdot10^7, 8\cdot10^8 Pa\ (s/m^3)^2$ In all cases, we assumed the tortuosity exponent in 6 $\beta_t = 0.5$.

For each value of f_p we consider as a reference a case with uniform f_t for all clusters providing additional $1MPa$ pressure drop at nominal rate (correspondingly, $f_t = 3.97\ 10^6 Pa\ (s/m^3)^{1/2}$ for 3 clusters, $f_t = 4.59\ 10^6 Pa\ (s/m^3)^{1/2}$ for 4 clusters) and a series of 4 realizations with f_t normally distributed around the same mean value with 20% dispersion ($\pm 0.2MPa$ at nominal rate).

In figures 10 - 16 we show fracture paths (top view), lengths, and fluid partitioning after 10 min. of injection into 4 fractures for equal $f_t = 4.59\ 10^6 Pa\ (s/m^3)^{1/2}$ in all clusters. In figures 11 - 18 we show fracture paths (top view), lengths, and fluid partitioning after 10 min. of injection into 4 fractures for two different realizations of varying f_t.

The averaged results over each set of realizations are provided in Tables 1 - 4.

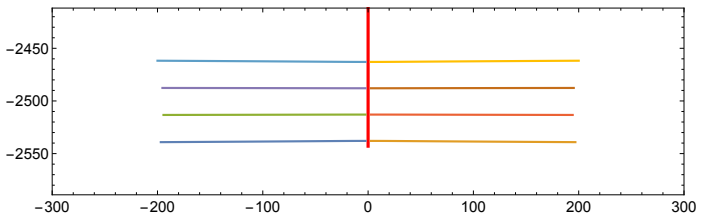

Fig. 10: Fracture paths (top view) after 10 minutes of injection. Equal f_t in all clusters, $f_p = 8 \cdot 10^7$. Scales in meters.

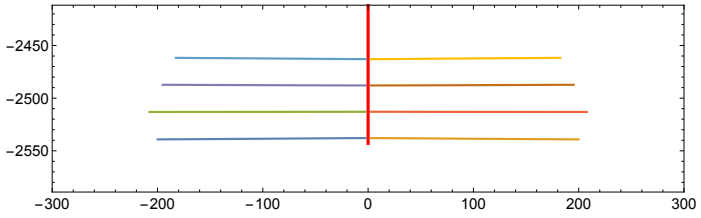

Fig. 11: Fracture paths (top view) after 10 minutes of injection. Varying f_t, case 1, $f_p = 8 \cdot 10^7$. Scales in meters.

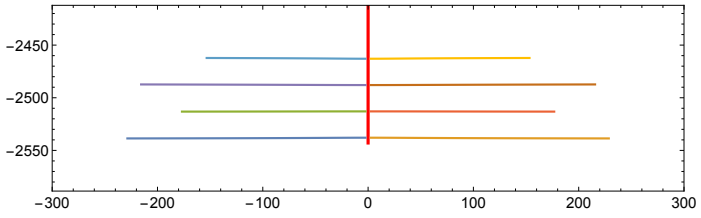

Fig. 12: Fracture paths (top view) after 10 minutes of injection. Varying f_t, case 2, $f_p = 8 \cdot 10^7$. Scales in meters.

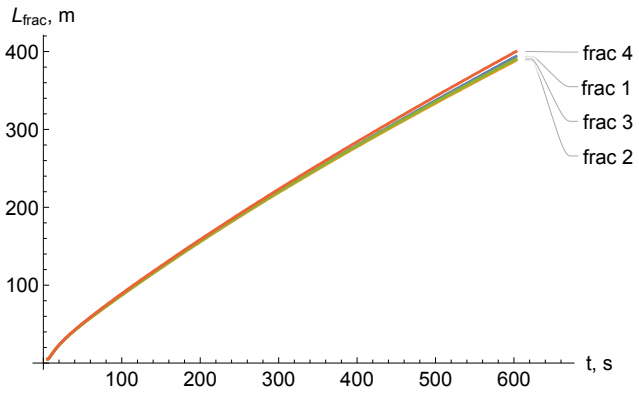

Fig. 13: Fractures' lengths during 10 minutes of injection. Equal f_t in all clusters, $f_p = 8 \cdot 10^7$.

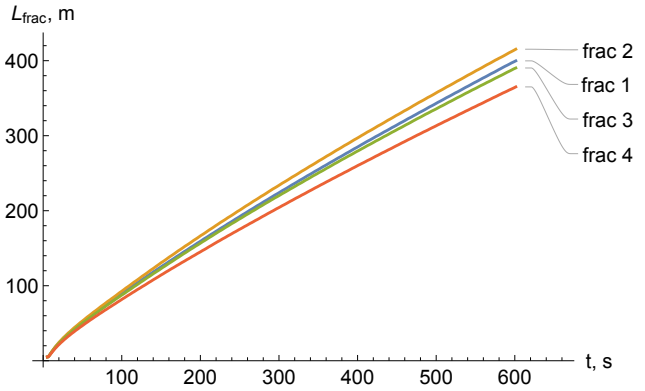

Fig. 14: Fractures' lengths during 10 minutes of injection. Varying f_t, case 1, $f_p = 8 \cdot 10^7$.

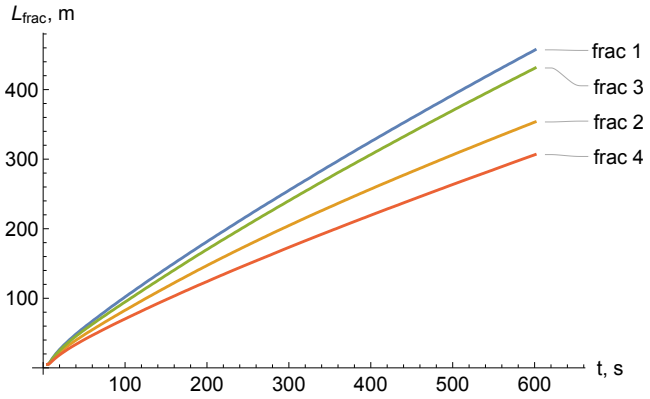

Fig. 15: Fractures' lengths during 10 minutes of injection. Varying f_t, case 2, $f_p = 8 \cdot 10^7$.

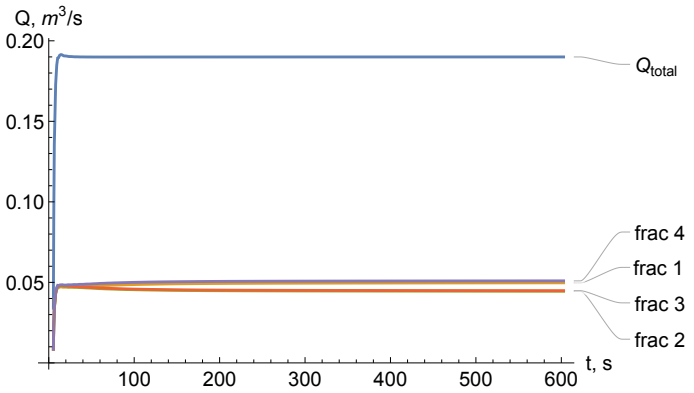

Fig. 16: Fluid partitioning during 10 minutes of injection. Equal f_t in all clusters, $f_p = 8 \cdot 10^7$.

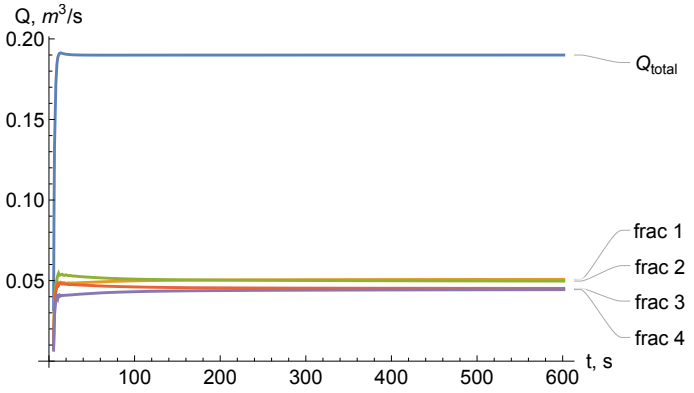

Fig. 17: Fluid partitioning during 10 minutes of injection. Varying f_t, case 1, $f_p = 8 \cdot 10^7$.

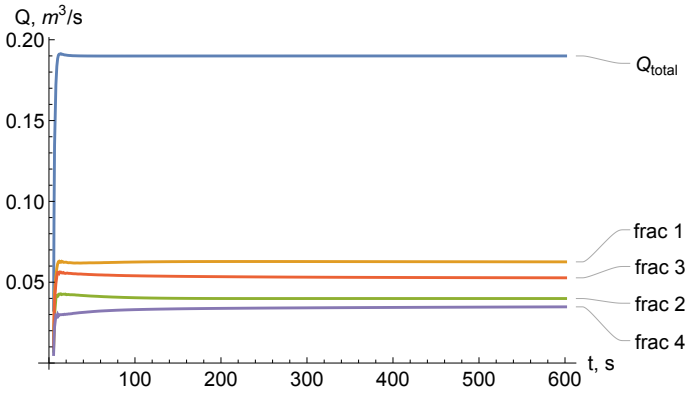

Fig. 18: Fluid partitioning during 10 minutes of injection. Varying f_t, case 2, $f_p = 8 \cdot 10^7$.

Table 1: Variation of fracture length, 3 clusters, comparison of equal f_t and varying f_t cases.

f_p	$8 \cdot 10^6$	$8 \cdot 10^7$	$8 \cdot 10^8$
$\delta L/\langle L \rangle$, equal f_t	0.02600	0.01271	0.01261
Average $\delta L/\langle L \rangle$, var. f_t	0.14201	0.10047	0.02815
Std. dev. of $\delta L/\langle L \rangle$, var. f_t	0.03651	0.05891	0.00821

Table 2: Variation of entry fluid volume rate, 3 clusters, comparison of equal f_t and varying f_t cases.

f_p	$8 \cdot 10^6$	$8 \cdot 10^7$	$8 \cdot 10^8$
$\delta Q/\langle Q \rangle$, equal f_t	0.09706	0.06977	0.01826
Average $\delta Q/\langle Q \rangle$, var. f_t	0.18917	0.14673	0.03945
Std. dev. of $\delta Q/\langle Q \rangle$, var. f_t	0.07593	0.08466	0.02639

Table 3: Variation of fracture length, 4 clusters, comparison of equal f_t and varying f_t cases.

f_p	$8 \cdot 10^6$	$8 \cdot 10^7$	$8 \cdot 10^8$
$\delta L/\langle L \rangle$, equal f_t	0.02414	0.00747	0.01224
Average $\delta L/\langle L \rangle$, var. f_t	0.12255	0.08514	0.02083
Std. dev. of $\delta L/\langle L \rangle$, var. f_t	0.02793	0.04948	0.00974

Table 4: Variation of entry fluid volume rate, 4 clusters, comparison of equal f_t and varying f_t cases.

f_p	$8 \cdot 10^6$	$8 \cdot 10^7$	$8 \cdot 10^8$
$\delta Q/\langle Q \rangle$, equal f_t	0.09706	0.06977	0.01826
Average $\delta Q/\langle Q \rangle$, var. f_t	0.18917	0.14673	0.03945
Std. dev. of $\delta Q/\langle Q \rangle$, var. f_t	0.07593	0.08466	0.02639

In Figs. 19 and 20 we plot the relative variation of the entry fluid volume rate $\delta Q/\langle Q \rangle$ (average over 4 realizations of varying f_t) compared to the variation of Q for equal f_t in all clusters against the parameters Γ_m and Π_β.

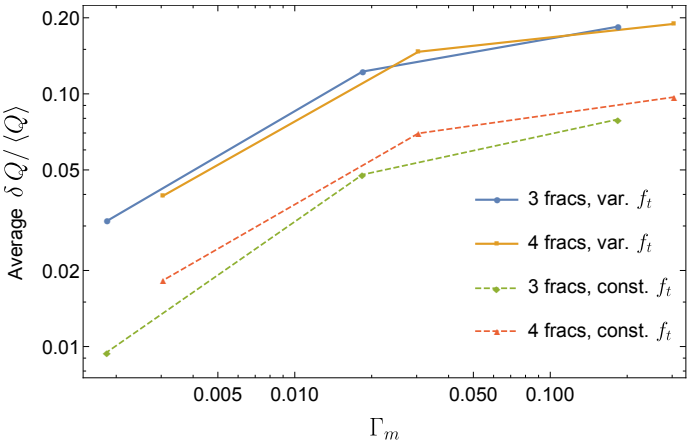

Fig. 19: Variation of entry fluid volume rate for different Γ_m.

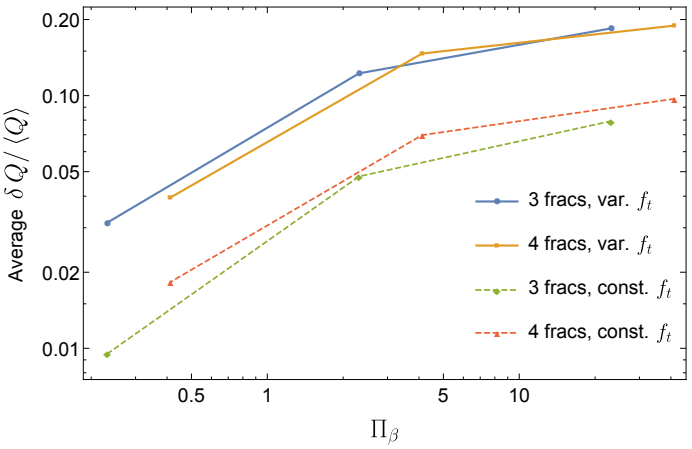

Fig. 20: Variation of entry fluid volume rate for different Π_β.

From Figs. 19 - 20 one can see that, on average, the variation of entry rate increased about 3 times compared to the homogeneous f_t case (equal tortuosity friction in all clusters) although the input variation of f_t was quite small (20%). Note that, although parameters Γ_m and Π_β have an expectable effect on fluid partitioning, the factor in $\delta Q/\langle Q\rangle$ due to the variation of f_t barely depends on these parameters.

6. CONCLUSIONS

Our results confirm previous studies restricted to the growth of simultaneous radial hydraulic fractures (see Lecampion and Desroches (2015b,a)) that were intrinsically confined to the early stage of growth. Notably, large entry friction appears to always allow to counteract the detrimental effect of stress interaction between fractures. Our results also show that the pressure drop along the stage (i.e. the length of the stage) has more impact than the stress interaction.

In all cases, large entry friction is beneficial. However, we have also shown that spatial variations of the entry friction between fractures / cluster - which are likely due to variation of near-wellbore fracture tortuosity - have a very important impact and detrimentally affect the fluid partitioning between fractures (more than a factor 2 difference compared to the spatially homogeneous case was observed for variation of entry friction as low as 20%). This has a profound practical impact as small variations in near-wellbore fracture geometry are bound to happen (see e.g. Lecampion *et al.* (2015) for discussions).

Acknowledgements

We would like to thank Total E&P for funding and permission to publish this work.

REFERENCES

1. Blasius, H., 1913. *Das Ähnlichkeitsgesetz bei Reibungsvorgängen in Flüssigkeiten*, Springer.

2. Bunger, A.P. and Lecampion, B., 2017. Four critical issues for successful hydraulic fracturing applications, *in:* X.T. Feng, ed., *Rock Mechanics and Engineering*, CRC Press/Balkema, vol. 5 (Surface and Underground Projects), chap. 16.

3. Bunger, A.P. and Peirce, A.P., 2014. Numerical simulation of simultaneous growth of multiple interacting hydraulic fractures from horizontal wells, *in: ASCE Shale Energy Engineering Conference*, Pittsburgh, PA: ASCE.

4. Churchill, S.W., 1977. Friction-factor equation spans all fluid-flow regimes, *Chemical engineering*, 84 (24), 91–92.

5. Crouch, S.L. and Starfield, A.M., 1983. *Boundary element methods in solid mechanics*, George Allen & Unwin.

6. Crump, J.B. and Conway, M., 1988. Effects of perforation-entry friction on bottomhole treating analysis, *J. Pet. Tech*, 1041–1049, SPE 15474.

7. Dontsov, E. and Peirce, A.P., 2015. A non-singular integral equation formulation to analyse multiscale behaviour in semi-infinite hydraulic fractures, *Journal of Fluid Mechanics*, 781, R1.

8. Dontsov, E. and Peirce, A.P., 2017. A multiscale implicit level set algorithm (ILSA) to model hydraulic fracture propagation incorporating combined viscous, toughness, and leak-off asymptotics, *Computer Methods in Applied Mechanics and Engineering*, 313, 53–84.

9. Economides, M.J. and Nolte, K.G., 2000. *Reservoir Stimulation*, John Wiley & Sons.

10. Garagash, D.I., Detournay, E., and Adachi, J.I., 2011. Multiscale tip asymptotics in hydraulic fracture with leak-off, *Journal of Fluid Mechanics*, 669, 260–297.

11. Haaland, S.E., 1983. Simple and explicit formulas for the friction factor in turbulent pipe flow, *Journal of Fluids Engineering, Transactions of the ASME*, 105 (1), 89–90.

12. Kresse, O. and Weng, X., 2018. Numerical modeling of 3d hydraulic fractures interaction in complex naturally fractured formations, *Rock Mechanics and Rock Engineering*, 51 (12), 3863–3881.

13. Kumar, D. and Ghassemi, A., 2016. 3D proroelastic simulation and analysis of multiple fracture propagation and refracturing of closely-spaced horizontal wells, *in: the 50th US Rock Mechanics/ Geomechanics Symposium*, Houston, Texas.

14. Lagrone, K.W. and Rasmussen, J.W., 1963. A new development in completion methods - the limited entry technique, *J. Pet. Tech*, 695–702, SPE 530, paper presented at SPE Rocky Mountain Regional Meeting, May 27–28, in Denver, Colo.

15. Lecampion, B., Bunger, A.P., and Zhang, X., 2018. Numerical methods for hydraulic fracture propagation: A review of recent trends, *Journal of Natural Gas Science and Engineering*, 49, 66–83.

16. Lecampion, B. and Desroches, J., 2015a. Robustness to formation geological heterogeneities of the limited entry technique for multi-stage fracturing of horizontal wells, *Rock Mechanics Rock Engineering*, 48 (6), 2637–2644.

17. Lecampion, B. and Desroches, J., 2015b. Simultaneous initiation and growth of multiple radial hydraulic fractures from a horizontal wellbore, *Journal of the Mechanics and Physics of Solids*, 82, 235–258.

18. Lecampion, B., Desroches, J., Weng, X., Burghardt, J., and Brown, E.T., 2015. Can we engineer better multistage horizontal completions? evidence of the importance of near-wellbore fracture geometry from theory, lab and field experiments, *in: SPE Hydraulic Fracturing Technology Conference*, SPE 173363.

19. Lecampion, B., Peirce, A.P., Detournay, E., Zhang, X., Chen, Z., Bunger, A.P., Detournay, C., Napier, J., Abbas, S., Garagash, D., and Cundall, P., 2013. The impact of the near-tip logic on the accuracy and convergence rate of hydraulic fracture simulators compared to reference solutions, *in: The International Conference for Effective and Sustainable Hydraulic Fracturing, May 20-22, Brisbane, Australia*.

20. Mogilevskaya, S.G., 2014. Lost in translation: Crack problems in different languages, *International Journal of Solids and Structures*, 51 (25), 4492–4503.

21. Nikuradse, J., 1950. *Laws of flow in rough pipes*, National Advisory Committee for Aeronautics Washington.

22. Olson, J.E. and Taleghani, A.D., 2009. Modeling simultaneous growth of multiple hydraulic fractures and their interaction with natural fractures, *in: SPE Hydraulic Fracturing Technology Conference and Exhibition*, Society of Petroleum Engineers, SPE 119739.

23. Peirce, A.P., 2016. Implicit level set algorithms for modelling hydraulic fracture propagation, *Philosophical Transactions of the Royal Society of London A: Mathematical, Physical and Engineering Sciences*, 374 (2078), 20150423.

24. Pham, K.H., Ravi-Chandar, K., and Landis, C.M., 2017. Experimental validation of a phase-field model for fracture, *International Journal of Fracture*, 205 (1), 83–101.

25. Protasov, I., Peirce, A., and Dontsov, E., 2018. Modeling constant height parallel hydraulic fractures with the Elliptic Displacement Discontinuity Method (EDDM), *in: 52nd US Rock Mechanics/Geomechanics Symposium*, ARMA 18–230.

26. Wu, K. and Olson, J.E., 2015. A simplified three-dimensional displacement discontinuity method for multiple fracture simulations, *International Journal of Fracture*, 193 (2), 191–204.

27. Yang, B.H. and Joseph, D.D., 2009. Virtual nikuradse, *Journal of Turbulence*, (10), N11.

28. Yang, S.Q., 2009. Drag reduction in turbulent flow with polymer additives, *Journal of Fluids Engineering*, 131 (5), 051301.

29. Yang, S.Q. and Dou, G., 2010. Turbulent drag reduction with polymer additive in rough pipes, *Journal of Fluid Mechanics*, 642, 279–294.